Wavenumber domain analyses of vibro-acoustic decoupling and noise attenuation in a plate-cavity system enclosed by an acoustic black hole plate

Xiaodong Wang,[1] Hongli Ji,[1] Jinhao Qiu,[1,a)] and Li Cheng[2]
[1]*State Key Laboratory of Mechanics and Control of Mechanical Structures, Nanjing University of Aeronautics and Astronautics, Nanjing, 210016, China*
[2]*Department of Mechanical Engineering, The Hong Kong Polytechnic University, Kowloon, Hong Kong, 999077, China*

(Received 31 January 2019; revised 16 May 2019; accepted 10 June 2019; published online 9 July 2019)

The acoustic black hole (ABH) effect is realized in thin plate structures with a decreasing thickness according to a power-law function, and offers potential applications for structure vibration damping enhancement and free-field noise radiation suppression. In this paper, a wavenumber domain method (WNDM) is proposed for the analysis of vibro-acoustic coupling and internal noise reduction mechanism of a pentahedral cavity enclosed by a flexible plate with a two-dimensional ABH indentation, subject to a point force excitation. The system response of the ABH plate-cavity is computed by a validated finite element model. The relationship between the space-averaged sound energy inside the cavity and the spectra of the structural displacement and the acoustic mode of the cavity is established. This allows revealing a dual physical mechanism behind the observed noise reduction: amplitude reduction and mismatching between the wavenumber spectra of the plate displacement and the acoustic field, which results in a weakened vibro-acoustic coupling. An additional configuration with an ABH embedded in an irregular pentagonal wall of the cavity is examined. Despite the increasing complexity in the geometry of the coupling interface and its coupling with the cavity, numerical analyses confirm the generality of the observed physical phenomena and the applicability of the proposed WNDM to more complex system configurations.
 https://doi.org/10.1121/1.5114821

[NJK] Pages: 72–84

I. INTRODUCTION

The study of acoustic black holes (ABHs) has received increasing attention in recent years.[1–5] Taking a one-dimensional ABH beam as an example, its local thickness reduces according to a power-law profile [in the form $h(x) = \varepsilon x^m$, $m \geq 2$] to enable a reduction in the local phase velocity of incident flexural waves, eventually to zero, as they approach the tapered edge. As a result, flexural waves are trapped at the tip area with no reflections in the ideal scenario. 2-D plates can also be tailored to produce similar phenomena, forming a kind of lens, which focuses the flexural vibration energy to the pit region. The resulting high energy concentration is conducive to various applications such as passive vibration control, energy harvesting, and sound radiation control.

A wide range of studies focusing on different aspects of ABH structures have been reported. One-dimensional ABH was machined on the trailing edges of turbo-fan blades to suppress their vibration.[6,7] A circular pit placed in one of the foci of an elliptical plate was investigated.[8] Ensembles of circular ABH indentations were used to damp the vibration of rectangular plates.[9] ABHs have also been explored for noise control applications. A representative work is the one using a plate containing six ABHs, which shows an obvious reduction in the sound radiation into a free space.[10] Up to now, most of previous work dealt with the free-field problems.[11–14] It is well accepted that the reduction of the radiation efficiency of ABH plates is the dominant mechanism behind the sound radiation reduction into free field. The ABH effect spreads the vibration energy out into higher wavenumber components, thus redistributing supersonic vibration energy into the subsonic region with a lower radiation capability.

As a different type of problem, cavity noise control is relevant to many practical problems.[15–17] The problem is challenging because of the complex coupling between the structural vibration and the enclosed acoustic field, as evidenced by the fact that the mere suppression of the structural vibration may not systematically lead to a sound reduction. The problem is different from the free-field problem in terms of physics because of the structure-acoustic coupling and the existence of a significantly large number of acoustic modes.[18]

The interaction between the structure and the enclosure plays a vital role in the sound generation inside a cavity. The usually weak acoustic damping inside the cavity promotes strong acoustic modal responses. The potential benefit of using ABH design for interior noise reduction was investigated in our previous work using a four ABH grid configuration.[19] The cavity configuration, however, was limited to a regular rectangular cavity in which modal coupling takes place in a very selective manner. In fact, in a cavity with simple regular geometry, both the structural modes and the acoustic modes take regular shapes at the interface, and their

a)Electronic mail: qiu@nuaa.edu.cn

coupling shows relatively simple patterns. Therefore, the conclusions drawn using simple geometries need to be further examined and assessed in a more general context. Meanwhile, the increasing complexity in the system coupling due to the increased system geometry calls for a more systematic analysis approach. This forms the basic motivation for the present work.

In this paper, the vibro-acoustic coupling and the internal noise reduction mechanism in a pentahedral cavity with a flexible ABH plate is investigated. The interior sound field is generated by and fully coupled with the vibration of the ABH plate subject to a point force excitation. Using two different configurations, system response is computed through a finite element model, following a procedure which was validated in a former study.[19]

A wavenumber domain method (WNDM) is proposed for the analysis of vibro-acoustic coupling behavior and the internal noise reduction mechanism, after deriving the relationship between the space-averaged sound energy inside the cavity and the spectra of the structural displacement and the acoustic mode of the cavity. Through Fourier transforms, the expressions in the spatial domain are transformed into the wavenumber domain. The wavenumber spectrum can be computed for an interested frequency range which allows decomposing the vibration into different wavenumber components. Informing on both the direction and the velocity of the wave propagation, wavenumber components not only facilitate the analysis and the characterization of complex systems, but also reflect the wave-field compression characteristics in the ABH structure. A similar technique has been explored for other applications such as energy harvesting[20] and free-field sound radiation.[12] In the present case, the WNDM is used for further revealing the underlying mechanisms of the ABH-induced interior noise reduction under a fully coupled vibro-acoustic context. Compared with the method based on the modal coupling coefficients,[19] the WNDM offers the advantage of examining the entire displacement field of the structure coupled with a specific acoustic mode. Numerical results indicate that the redistribution of the displacement spectrum in the wavenumber domain induced by local vibration modes in the ABH structure is the main reason leading to the noise reduction in the cavity. It is also shown that the WNDM is effective for the coupling analysis of an irregular plate-cavity system.

The paper is organized as follows. The basic configuration is introduced in Sec. II. In Sec. III, the proposed WNDM is presented. A finite element model considering the full cavity-plate coupling is established in Sec. IV. In Sec. V, wavenumber domain analysis is carried out based on the finite element (FE) method simulation results. After showing some typical phenomena in the wavenumber domain, ABH effects on the plate-cavity coupling are scrutinized. Finally, the main work and conclusions are summarized in Sec. VI.

II. VIBRO-ACOUSTIC MODEL

The model under investigation consists of a pentahedral cavity-plate system as shown in Fig. 1(a). One of the cavity walls is covered by a flexible plate, while others are being considered as acoustically rigid. The size and shape of the system are shown in Fig. 1. For comparison, two types of

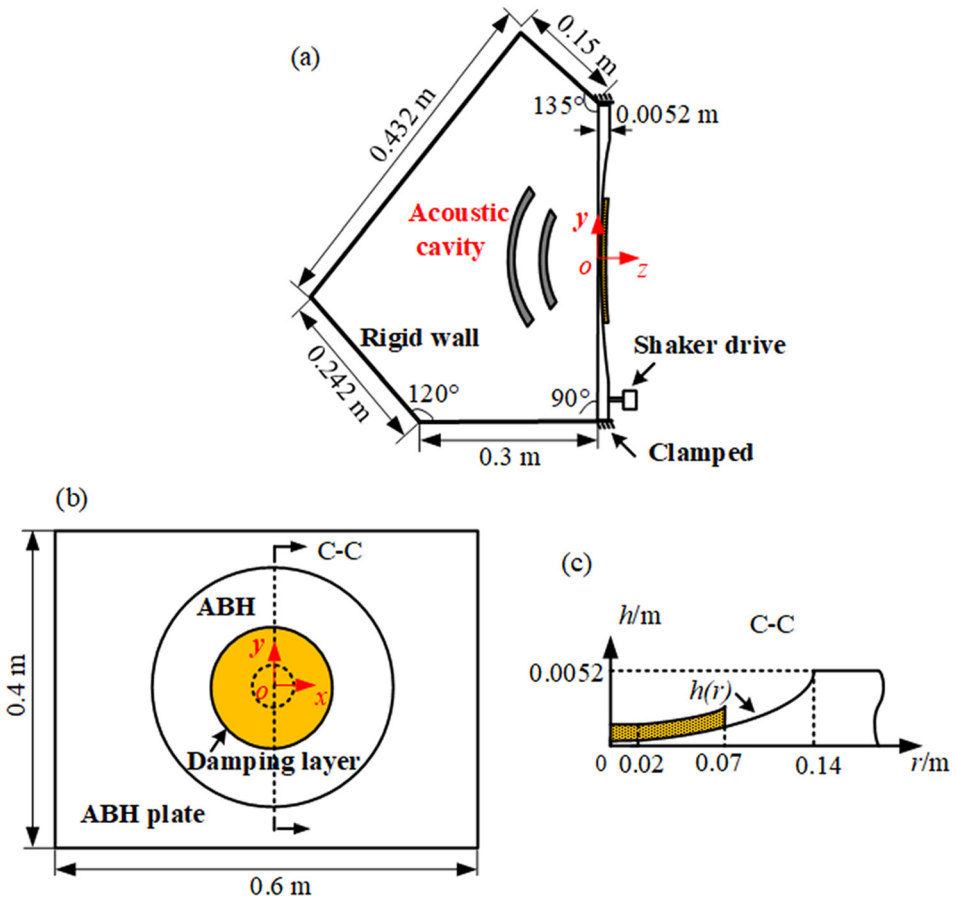

FIG. 1. (Color online) The configuration of the vibro-acoustic cavity system.

flexible plates, one with two-dimensional (2-D) ABH indentations (called ABH-plate) and the other without ABHs (called uniform plate) are investigated. Both plates are made of steel with the same dimension of $600 \times 400 \times 5.2$ mm, which are clamped to the edges of the cavity. Considering the engineering applicability and limited machining precision, a modified 2-D ABH cell with a profile proposed by Huang *et al.*[21] is embedded in the middle of the plate. The ABH indentation consists of a tapered region and a plateau with a constant thickness at its center, as shown in Fig. 1(b), whose thickness profile is described as

$$h(r) = \begin{cases} 0.0002, & r \le 0.02 \\ 0.3472(r-0.02)^2 + 0.0002, & 0.02 \le r \le 0.14, \end{cases} \tag{1}$$

where r is the radial distance from the center of the ABH indentation in a polar coordinate system. A circular butyl rubber constrained damping layer with a thickness of 0.002 m and a diameter of 0.07 m is bonded to the central area of the ABH indentation.

III. WAVENUMBER DOMAIN ANALYSIS THEORY

The discretized vibro-acoustic coupling equation of the plate-cavity system is cast into a standard form and detailed in the Appendix. The mean quadratic velocity of the plate defined in Eq. (A2) and the quadratic space-averaged sound energy inside the enclosure defined in Eq. (A3) are used to evaluate the vibration level of the plate and the sound field inside the cavity, respectively.[19] Equations (A11)–(A13) show that the complex amplitude of the ith acoustic mode depends on the coupling coefficient, C_i, between this acoustic mode and the displacement field over the plate–cavity interface, which includes the contribution from all the structural modes. Equation (A15) shows that the quadratic space-averaged sound pressure in the cavity is directly determined by the squared modulus of the coupling coefficient, $C_i C_i^*$. It should be noted that the coupling coefficient C_i, defined in this paper, is different from the modal coupling coefficient between the acoustic modes and the structural modes, defined in Ref. 19.

To perform the wavenumber domain analysis, the relationship between the coupling coefficient and the displacement spectra in the wavenumber domain needs to be established. According to Eq. (A13), the product of the coupling coefficient and its conjugate can be written as

$$\begin{aligned} C_i C_i^* &= \int\int \left[\tilde{w}_n^{\mathrm{Re}}(x,y) + \imath \tilde{w}_n^{\mathrm{Im}}(x,y)\right] \hat{\psi}_i(x,y)\, dx\, dy \\ &\quad \times \int\int \left[\tilde{w}_n^{\mathrm{Re}}(x,y) - \imath \tilde{w}_n^{\mathrm{Im}}(x,y)\right] \hat{\psi}_i(x,y)\, dx\, dy \\ &= \left(\int\int \tilde{w}_n^{\mathrm{Re}}(x,y)\hat{\psi}_i(x,y)\, dx\, dy\right)^2 \\ &\quad + \left(\int\int \tilde{w}_n^{\mathrm{Im}}(x,y)\hat{\psi}_i(x,y)\, dx\, dy\right)^2 = C_1^2 + C_2^2, \end{aligned} \tag{2}$$

where

$$\begin{aligned} C_1 &= \int\int \tilde{w}_n^{\mathrm{Re}}(x,y)\hat{\psi}_i(x,y)\, dx\, dy, \\ C_2 &= \int\int \tilde{w}_n^{\mathrm{Im}}(x,y)\hat{\psi}_i(x,y)\, dx\, dy. \end{aligned} \tag{3}$$

The cross correlation of $\tilde{w}_n^{\mathrm{Re}}(x,y)$ and $\hat{\psi}_i(x,y)$ is defined by

$$\begin{aligned} \mathcal{C}_1(x,y) &= \int\int \tilde{w}_n^{\mathrm{Re}}(\xi,\eta)\hat{\psi}_i(\xi+x,\eta+y)\, d\xi\, d\eta \\ &= \tilde{w}_n^{\mathrm{Re}}(x,y) * \hat{\psi}_i(-x,-y), \end{aligned} \tag{4}$$

where "*" represents the convolution of two functions.

Based on the convolution integral theorem, Eq. (4) can be expressed in the following form in the wavenumber domain as

$$\mathcal{C}_1(k_x,k_y) = \tilde{w}_n^{\mathrm{Re}}(k_x,k_y)\hat{\psi}_i^*(k_x,k_y), \tag{5}$$

where

$$\begin{aligned} \tilde{w}_n^{\mathrm{Re}}(k_x,k_y) &= \int\int \tilde{w}_n^{\mathrm{Re}}(x,y)e^{-\imath k_x x}e^{-\imath k_y y}dx\, dy, \\ \tilde{\psi}_i(k_x,k_y) &= \int\int \tilde{\psi}_i(x,y)e^{-\imath k_x x}e^{-\imath k_y y}dx\, dy, \end{aligned} \tag{6}$$

where k_x and k_y are the wavenumbers in the x and y directions, respectively. It should be noted that the same symbols are used to denote the same function in both the spatial domain and wavenumber domain.

The original function $\mathcal{C}_1(x,y)$ in the spatial domain can be obtained from $\mathcal{C}_1(k_x,k_y)$ in the wavenumber domain by 2-D inverse Fourier transform as

$$\mathcal{C}_1(x,y) = \frac{1}{(2\pi)^2}\int\int \mathcal{C}_1(k_x,k_y)e^{i(k_x x + k_y y)}dk_x\, dk_y. \tag{7}$$

Obviously, there exists

$$\begin{aligned} C_1 = \mathcal{C}_1(0,0) &= \frac{1}{(2\pi)^2}\int\int \mathcal{C}_1(k_x,k_y)\, dk_x\, dk_y \\ &= \frac{1}{(2\pi)^2}\int\int \tilde{w}_n^{\mathrm{Re}}(k_x,k_y)\hat{\psi}_i^*(k_x,k_y)\, dk_x\, dk_y. \end{aligned} \tag{8}$$

Similar relationships hold for C_2 in Eq. (3). These results indicate that the spectra $\tilde{w}_n^{\mathrm{Re}}(k_x,k_y)$, $\tilde{w}_n^{\mathrm{Im}}(k_x,k_y)$, and $\hat{\psi}_i(k_x,k_y)$ in the wavenumber domain can be used to evaluate the coupling coefficient and explain the changes in the acoustic field inside the cavity.

When the plate is excited at the resonance frequency of the ith acoustic mode, the amplitude of normal velocity of the plate can be expressed as

$$v_n = \imath\omega_{ai}\tilde{w}_n(x,y) = \imath\omega_{ai}\sum_j \tilde{q}_{sj}\hat{\varphi}_j(x,y). \tag{9}$$

Based on the same principle of wavenumber-domain analysis used above, the mean quadratic velocity defined in Eq. (A2) can be calculated from the spectrum of $\tilde{w}_n$ as

$$\overline{\langle v_n^2 \rangle} = \frac{\omega_{ai}^2}{8\pi^2 S}\left[\int\int |\tilde{w}_n(k_x,k_y)|^2 dk_x\, dk_y\right]$$
$$= \frac{\omega_{ai}^2}{8\pi^2 S}\left[\int\int |\tilde{w}_n^{\mathrm{Re}}(k_x,k_y)|^2 dk_x\, dk_y + \int\int |\tilde{w}_n^{\mathrm{Im}}(k_x,k_y)|^2 dk_x\, dk_y\right]. \quad (10)$$

The above expression suggests that $|\tilde{w}_n(k_x,k_y)|$ is directly related to the mean quadratic velocity.

The above results also indicate that the reduction in the quadratic space-averaged sound pressure can be induced by a reduction of $|\tilde{w}_n(k_x,k_y)|$ due to vibration suppression and a decrease in the degree of matching between $\tilde{w}_n(k_x,k_y)$ and $\hat{\psi}_i(k_x,k_y)$. Obviously, the product of $\tilde{w}_n(k_x,k_y)$ and $\hat{\psi}_i(k_x,k_y)$ in Eq. (8) will be small if there is significant mismatching in wavenumber between these two functions.

IV. FE MODEL AND SIMULATION

A FE numerical model is established, following the modeling procedure which has been verified by experiments in an early work.[19] The FE model is built based on the three-dimensional elastic theory in conjunction with the acoustic field description, with a view to reveal the physical phenomena on one hand, and explore the underlying physical mechanism on the other hand. The ABH plate is discretized using C3D20 solid elements in ABAQUS (dassault SIMULIA Inc., Providence, RI), which is a second-order element with 20 nodes. The frequency range is from 100 to 5000 Hz. Finer meshes are used in the central area of the ABHs to ensure more than ten elements per local wavelength at twice the maximum frequency of interest, as shown in Fig. 2. The total number of elements for the ABH-plate is 38032. The viscoelastic damping layer and the metal part of the plate are connected by a common node technique. A uniform plate (without ABH) of the same size (coated with the same amount of damping layer at the same corresponding location), used as reference, is also modeled using the same method. Material parameters of the plate and those of the damping layers are tabulated in Table I. The mesh grid with eight nodes is used for acoustic analysis of the cavity. The mesh generation leads to more than six elements per local acoustic wavelength to guarantee the computation accuracy. The interaction between the plate and the acoustic field is realized by a coupling surface, which establishes data mapping without the need of matching between the structural mesh of the plate and the cavity mesh for the acoustic field. In addition, a convergence verification is also performed to ensure the accuracy and reliability of the simulation results.

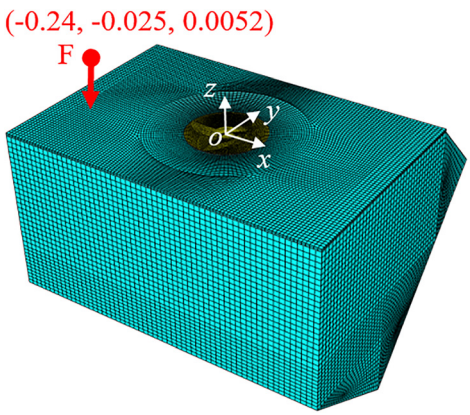

FIG. 2. (Color online) The FE model of the vibro-acoustic cavity system.

TABLE I. Material properties of the plate and the damping layer.

Plate	Damping layer
$E_p = 206\,\mathrm{GPa}$	$E_d = 0.1\,\mathrm{GPa}$
$\rho_p = 7850\,\mathrm{kg/m^3}$	$\rho_d = 1780\,\mathrm{kg/m^3}$
$\nu_p = 0.28$	$\nu_d = 0.45$
$\eta_p = 0.004$	$\eta_d = 0.28$

A transverse harmonic driving force of unit amplitude (1 N) is applied to both panels at $(-0.24, -0.025, 0.0052)$ as shown in Fig. 2. In the FE model, a modal loss factor of 0.001 is assigned to all acoustic modes, as used in Eq. (A6). The modal loss factors of the plates can be gained through complex modal analysis. Figure 3 shows the modal loss factors for the ABH plate and uniform reference plate. It can be seen that the loss factors of the ABH plate are systematically increased compared with those of the uniform plate as a result of ABH-induced enhancement of the system damping.

V. RESULTS AND DISCUSSIONS

A. Vibration and noise reduction phenomena

System responses are computed using the FE model described in Sec. IV with the help of commercial finite element code ABAQUS and VIRTUAL.LAB (Siemens PLM Software, LMS, Belgium).

The mean quadratic velocities of both plates (the rectangular ABH-plate and rectangular uniform plate) under the same mechanical excitation are shown in Fig. 4(a). The first resonance frequencies of the ABH-plate and uniform plate are 252.18 Hz and 212.74 Hz, respectively. The frequency of the first local resonance mode of the ABH plate is 429.75 Hz, which is below its characteristic frequency, 642 Hz. ABH-induced vibration attenuation of the plate is similar to the observations reported in the literature.[7–9,22,23]

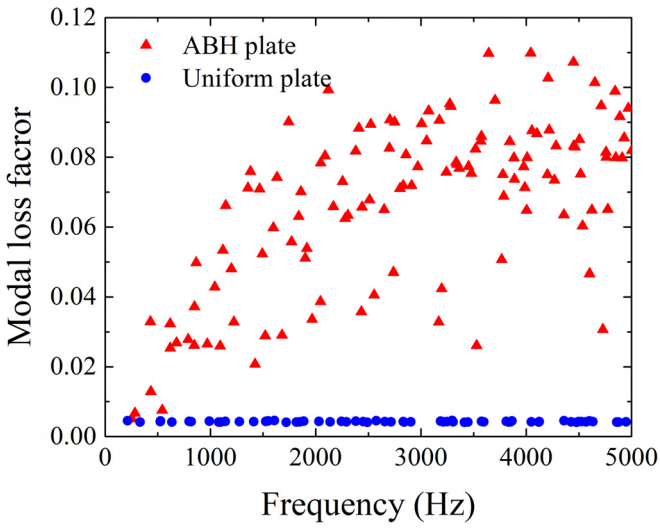

FIG. 3. (Color online) Modal loss factor of the ABH plate vs uniform plate.

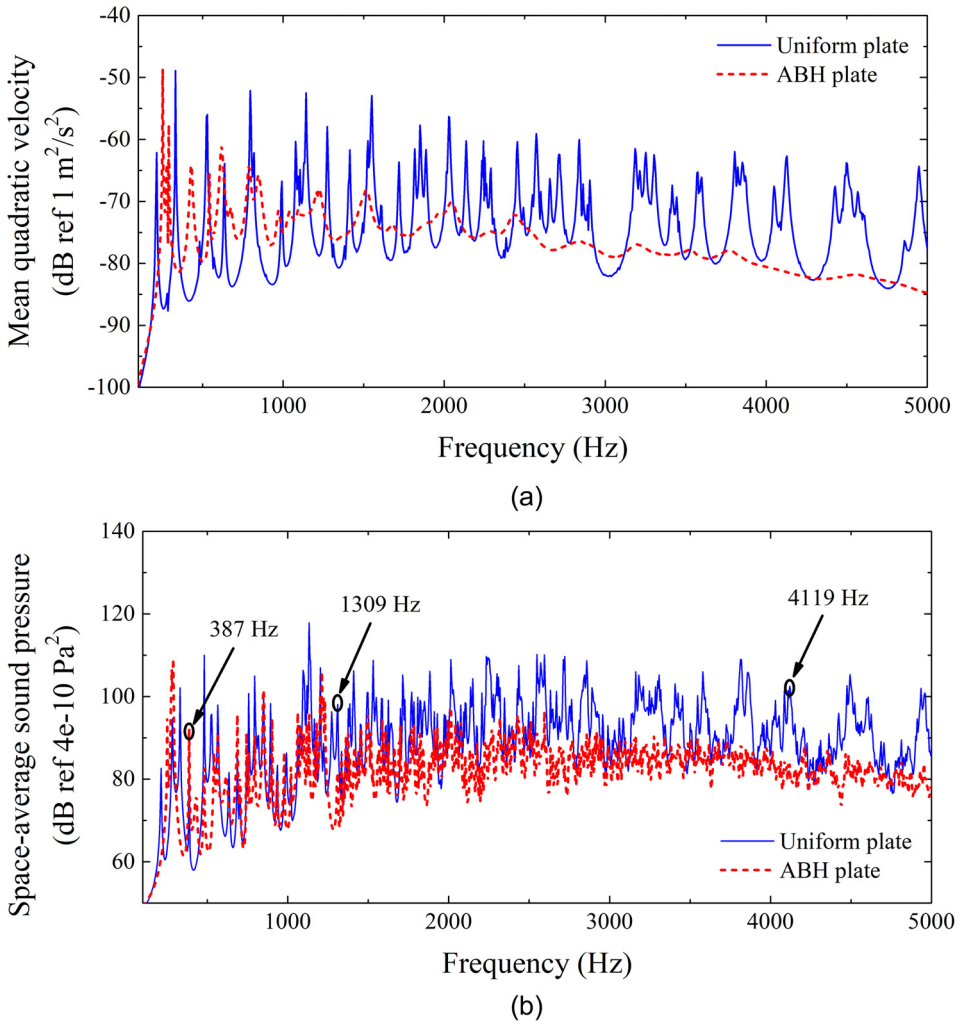

FIG. 4. (Color online) Comparisons between the uniform plate and the ABH plate in narrow band. (a) Mean quadratic velocity of the plate. (b) Quadratic space-average sound pressure level of the cavity.

The excellent vibration attenuation performance is mainly attributed to the increase in the overall system damping due to the superior energy trapping capability of the ABH indentation. The vibration level of the ABH plate is significantly reduced mainly at frequencies above 430 Hz, compared with its uniform counterpart. Reductions range from 5 to 30 dB at the resonance frequencies above 430 Hz. However, no obvious reductions can be observed in the low frequency range.

The mechanism of vibration reduction in ABH structures has been revealed in the former studies.[11,19] Systematic ABH effects can only be expected above a cut-on frequency when local modes appear in the ABH region. Above the cut-on frequency, structural modes are mainly dominated by local deformation within the ABH indentation except for a few global vibration modes, and their modal loss factors of local resonance modes are significantly increased as compared with the uniform plate as shown in Fig. 3. Therefore, there is no sharp peak in the high frequency range because the vibration energy can be effectively dissipated by the damping layer. Instead, in the low frequency range, the vibration is mainly contributed by the global modes, where the vibration amplitude is generally higher than that of the uniform plate because the total mass of the ABH plate is 13.5% less than that of the uniform plate due to the ABH indentation, which results in the weakening of the structural stiffness.

The acoustic benefit inside the cavity caused by the ABH plate is investigated and compared with its uniform counterpart. The quadratic space-averaged sound pressures inside the cavity of the ABH-plate and uniform plate are calculated with results shown in Fig. 4(b). It can be seen that the sound pressure in the cavity is reduced for the ABH plate in a wide frequency range, compared with the case of the uniform plate. The reduction is again more obvious and systematic at the frequency above 430 Hz where the ABH are apparently more effective. It means that the sound waves cannot be effectively radiated into the cavity for the ABH plate when frequency is beyond cut-on frequency. In the low frequency band, the noise reduction cannot be achieved due to the weakening of the structural stiffness.

The overall effect of the ABH on the dynamics of the system in one-third octave bands is shown in Fig. 5, displaying a reduction in the plate vibration by 2–10 dB above 400 Hz, except the band centered at 630 Hz. A noise reduction, ranging from 2 to 20 dB, can be observed in the frequency above 400 Hz in Fig. 5(b). Note that the noise level reduction exceeds that of the vibration level at some frequencies. This observation confirms the observation made previously[19] that apart from the added damping effect, there exist other effects on the structural radiation imposed by the ABH indentation.

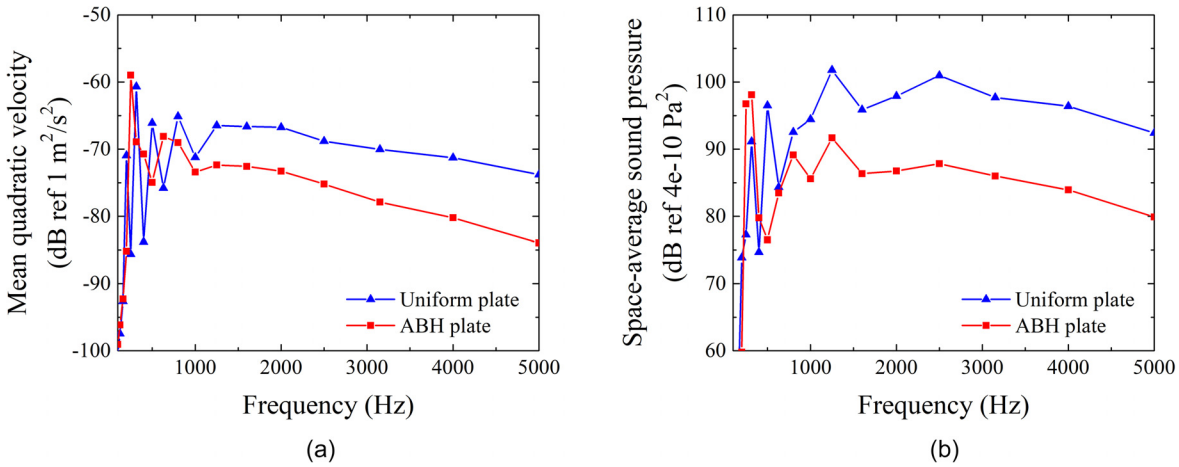

FIG. 5. (Color online) Comparisons between the uniform plate and the ABH plate in one-third octave bands. (a) Mean quadratic velocity of the plate. (b) Quadratic space average sound pressure level of the cavity.

B. Analyses of control mechanisms using wavenumber domain method

Three typical acoustic resonance frequencies, 387 Hz, 1309 Hz, and 4119 Hz as shown in Fig. 4(b), are considered to explain the observed phenomena. The mean quadratic velocity, quadratic space-averaged sound pressure of the ABH plate-cavity, and the uniform plate-cavity at these frequencies are listed in Table II. Meanwhile, differences of these quantities between the two systems are also listed in Table II. At a low frequency (387 Hz), mean quadratic velocity and quadratic space-averaged sound pressure of the ABH plate-cavity are increased by 6.3 dB and 4.8 dB, respectively. At the medium frequency (1309 Hz), the vibration of the ABH plate is similar to that of the uniform plate. However, ABH presents an obvious beneficial effect in terms of noise reduction. At the higher frequency (4119 Hz), the vibration and noise of the system with an ABH are greatly reduced.

The results in Table II indicate obviously different mechanisms of vibration attenuation and noise reduction. In the former study,[19] the coupling coefficients between a given acoustic mode and the structural modes were used to explain the mechanism of noise reduction at the resonance frequency of the given acoustic mode. However, because each acoustic mode is excited by multiple structural modes, explanation based on coupling coefficients was not intuitive. In this study, the wavenumber domain analysis is used.

As discussed in Sec. III above, the reduction in $C_iC_i^*$ can be attributed to the reduction of $|\tilde{w}_n(k_x,k_y)|$, the decrease in the degree of matching between $\tilde{w}_n(k_x,k_y)$ and $\hat{\psi}_i(k_x,k_y)$, or both of them. The spectra $\tilde{w}_n^{\mathrm{Re}}(k_x,k_y)$, $\tilde{w}_n^{\mathrm{Im}}(k_x,k_y)$, $\hat{\psi}_i(k_x,k_y)$ in Eq. (6) and their product defined in Eq. (5) are calculated and used to explain the mechanism behind the observed noise reduction.

TABLE II. Vibration and noise reduction at the typical frequencies.

Frequency (Hz)	Mean quadratic velocity (dB)			Space-averaged sound pressure (dB)		
	ABH	Uniform	Difference	ABH	Uniform	Difference
387	−78.6	−84.9	+6.3	92.2	87.4	+4.8
1309	−76.2	−76.9	+0.7	81.5	98.1	−16.6
4119	−81.4	−64.7	−16.7	83.8	102.5	−18.7

At the three discrete frequencies tabulated in Table II, $\tilde{w}_n^{\mathrm{Re}}(k_x,k_y)$, $\tilde{w}_n^{\mathrm{Im}}(k_x,k_y)$ of both plates, and $\hat{\psi}_i(k_x,k_y)$ of the cavity are calculated using the discrete Fourier transform implementation of Eq. (4), and their modulus are plotted in Figs. 6, 8, and 10, respectively. Considering the relationship between the wavelength λ and the wavenumber k, $\lambda = 2\pi/k$, λ decreases, and k increases when frequency increases. The local vibration modes inside an ABH also have small wavelength λ and large wavenumber k.

Equations (2) and (3) show that the value of $C_iC_i^*$ depends on C_1 and C_2, which in turn depends on the product of $\tilde{w}_n^{\mathrm{Re}}(k_x,k_y)$ and $\hat{\psi}_i(k_x,k_y)$ and that of $\tilde{w}_n^{\mathrm{Im}}(k_x,k_y)$ and $\hat{\psi}_i(k_x,k_y)$. These products at the three frequencies in Table II are calculated and plotted in Figs. 7, 9, and 11 for both the ABH plate-cavity and uniform plate-cavity. It is obvious that the products not only depend on the value of $\tilde{w}_n^{\mathrm{Re}}(k_x,k_y)$ and $\tilde{w}_n^{\mathrm{Im}}(k_x,k_y)$, but also the degree of their morphological matching with $\hat{\psi}_i(k_x,k_y)$ in the wavelength domain.

The abovementioned results are further discussed for the three frequencies. At 387 Hz, which is below the resonance frequency of the first local ABH mode, the plate vibration is dominated by the global modes and the ABH effect is not apparent. The real and imaginary parts of the ABH plate displacement are larger than those of the uniform plate displacement, as shown in Figs. 6(a)–6(d), due to the reduced mass and stiffness of the former. The degree of morphological matching between the real and imaginary parts of the displacement field and the acoustic mode of the ABH-plate, shown in Fig. 6(e), is slightly higher than that between the structural mode of the uniform plate and the acoustic mode. The products of the spectra are shown in Fig. 7 for both the ABH plate and uniform plate. Because the magnitudes of $\tilde{w}_n^{\mathrm{Re}}(k_x,k_y)$ and $\tilde{w}_n^{\mathrm{Im}}(k_x,k_y)$ of the ABH plate are larger than those of the uniform plate, the magnitudes of the products $\mathcal{C}_1(k_x,k_y) = \tilde{w}_n^{\mathrm{Re}}(k_x,k_y)\hat{\psi}_i^*(k_x,k_y)$ and $\mathcal{C}_2(k_x,k_y) = \tilde{w}_n^{\mathrm{Im}}(k_x,k_y)\hat{\psi}_i^*(k_x,k_y)$ of the ABH plate-cavity are also larger than those of the uniform plate-cavity. For quantitative comparison, the numerical integration is performed on

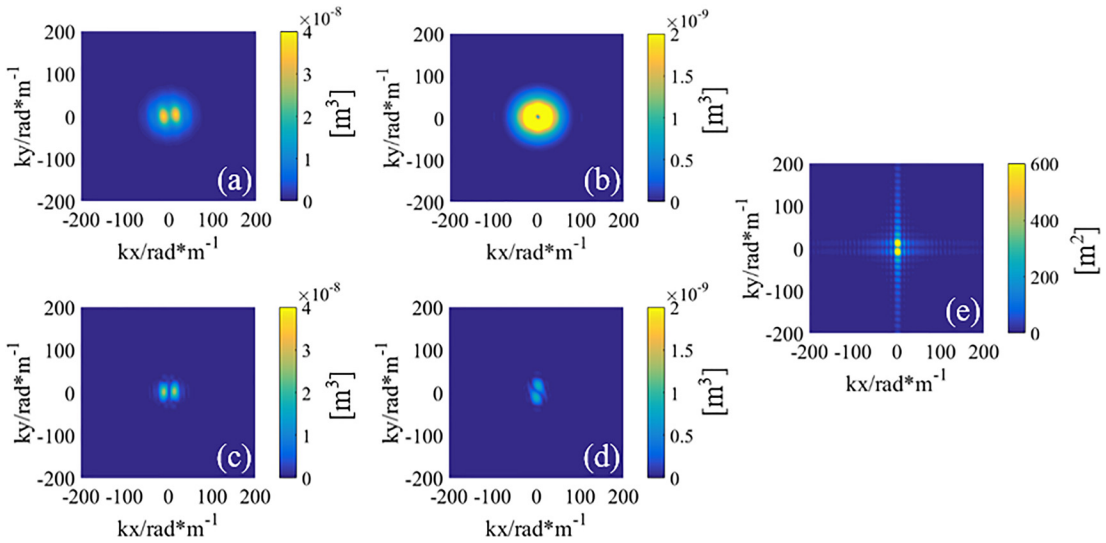

FIG. 6. (Color online) The modulus of wavenumber-domain spectra of the displacements and acoustic mode at 387 Hz. (a) and (b) correspond to the real and imaginary parts of ABH plate displacement, respectively; (c) and (d) correspond to the real and imaginary parts of uniform plate displacement, respectively; (e) corresponds to the acoustic modal vector at the interface.

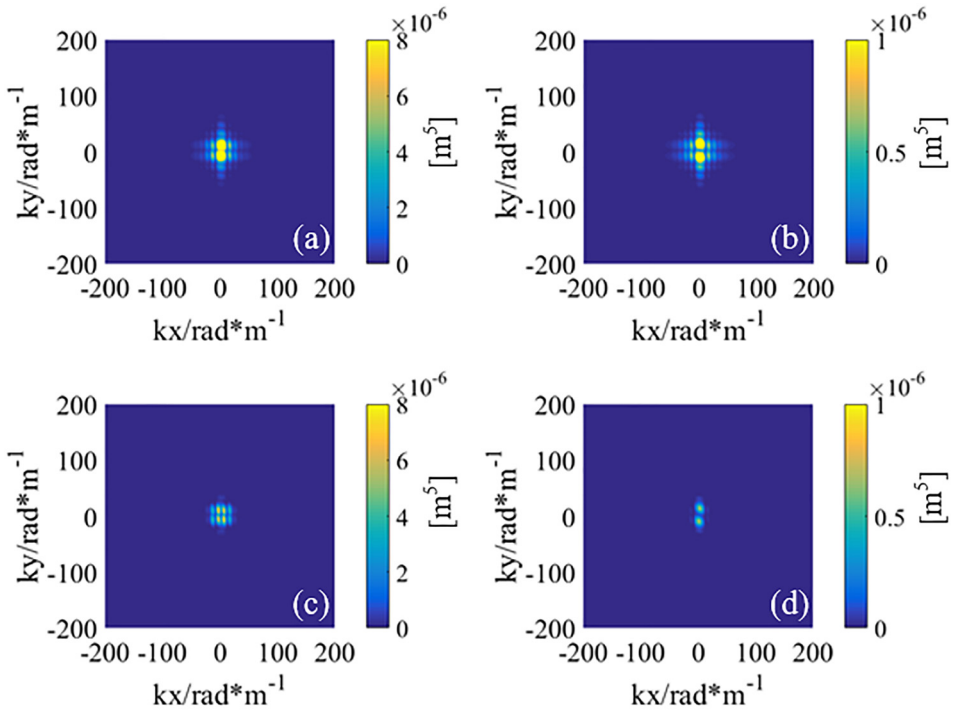

FIG. 7. (Color online) The modulus of wavenumber-domain spectra of the cross-correlation function at 387 Hz. (a) and (b) correspond to the real and imaginary parts, respectively, of ABH plate displacement with acoustic modal vector at interface; (c) and (d) correspond to the real and imaginary parts, respectively, of uniform plate displacement with acoustic modal vector at interface.

TABLE III. The coupling coefficient at the typical frequencies.

	ABH plate			Uniform plate		
Frequency (Hz)	Real (10^{-7} m^3)	Imaginary (10^{-7} m^3)	Amplitude (10^{-7} m^3)	Real (10^{-7} m^3)	Imaginary (10^{-7} m^3)	Amplitude (10^{-7} m^3)
387	5.32	7.71	9.37	4.81	2.44	5.39
1309	9.32	2.20	9.58	64.07	11.26	65.05
4119	1.83	1.13	2.15	14.64	3.76	15.12

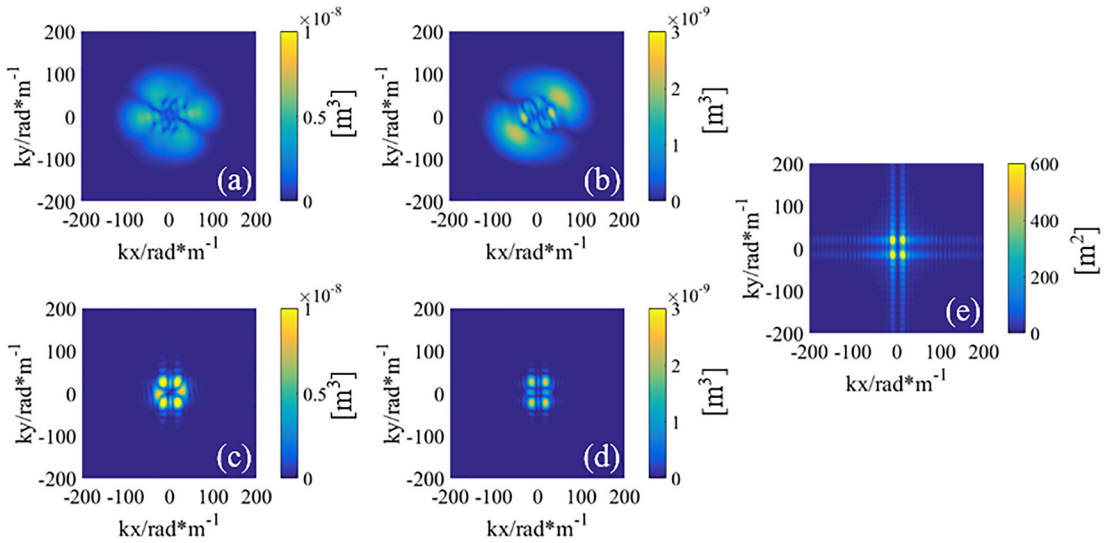

FIG. 8. (Color online) The modulus of wavenumber-domain spectra of the displacements and acoustic mode at 1309 Hz. (a) and (b) correspond to the real and imaginary parts, respectively, of ABH plate displacement; (c) and (d) correspond to the real and imaginary parts, respectively, of uniform plate displacement; (e) corresponds to the acoustic modal vector at the interface.

Eq. (8) and the calculated values of C_1, C_2, and $\sqrt{CC^*} = \sqrt{C_1^2+C_2^2}$ are listed in Table III. Obviously, the value of $\sqrt{C_1^2+C_2^2}$ of the ABH plate-cavity is 1.74 times that of the uniform plate-cavity.

Following the same logic and examining the modulus of wavenumber-domain spectra of the displacement of both plates at 1309 Hz (away from the resonance frequencies of both plates), Figs. 8(a) and 8(b) show that more low wavenumber energy is spread into high wavenumber components, exhibiting more complex pattern than the uniform plate. This is understandable because above the cut-on frequency, flexural waves are compressed alongside a wavelength decrease, resulting in obvious energy trapping inside the ABH area. For the uniform plate, the wavenumber components are only concentrated near the modal wavenumber components as shown in Figs. 8(c) and 8(d).

The products of the spectra are shown in Fig. 9 for both the ABH plate and the uniform plate. Although the vibration amplitude of the ABH plate is slightly larger than that of the uniform plate at 1309 Hz frequency as shown in Table II, the distribution of vibration response in the ABH plate undergoes significant changes due to the compressed and localized feature of the ABH effect, which in turn reduces the sound pressure inside the cavity as a result of weakened matching strength between the surface displacement field of the ABH plate and acoustic modal vector at the interface. This implies

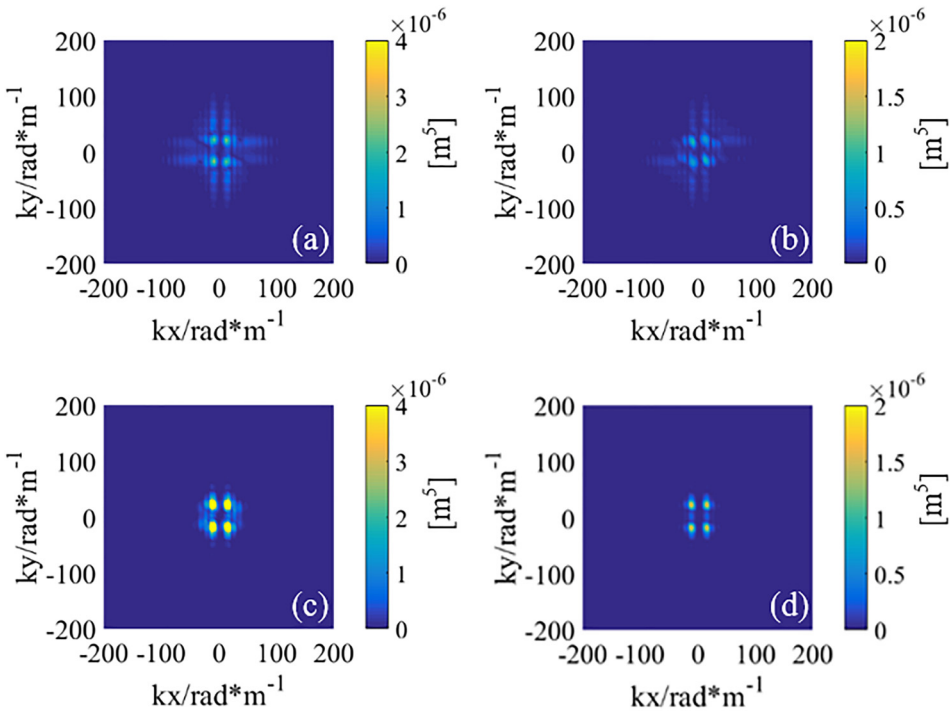

FIG. 9. (Color online) The modulus of wavenumber-domain spectra of cross-correlation function at 1309 Hz. (a) and (b) correspond to the real and imaginary parts, respectively, of ABH plate displacement with acoustic modal vector at interface; (c) and (d) correspond to the real and imaginary parts, respectively, of uniform plate displacement with acoustic modal vector at interface.

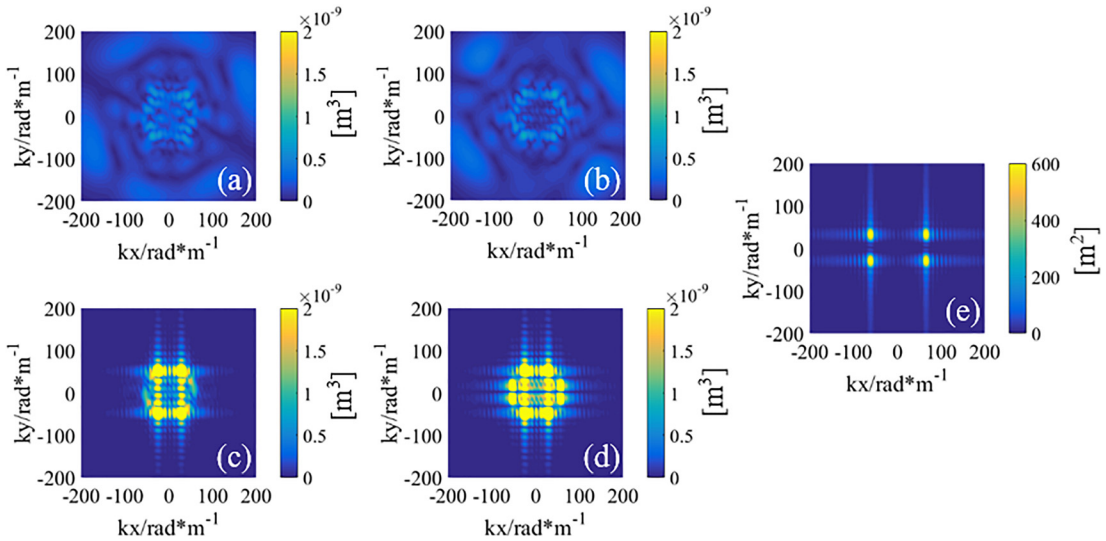

FIG. 10. (Color online) The modulus of wavenumber-domain spectra of the displacements and acoustic mode at 4119 Hz. (a) and (b) correspond to the real and imaginary parts, respectively, of ABH plate displacement; (c) and (d) correspond to the real and imaginary parts, respectively, of uniform plate displacement; (e) corresponds to the acoustic modal vector at the interface.

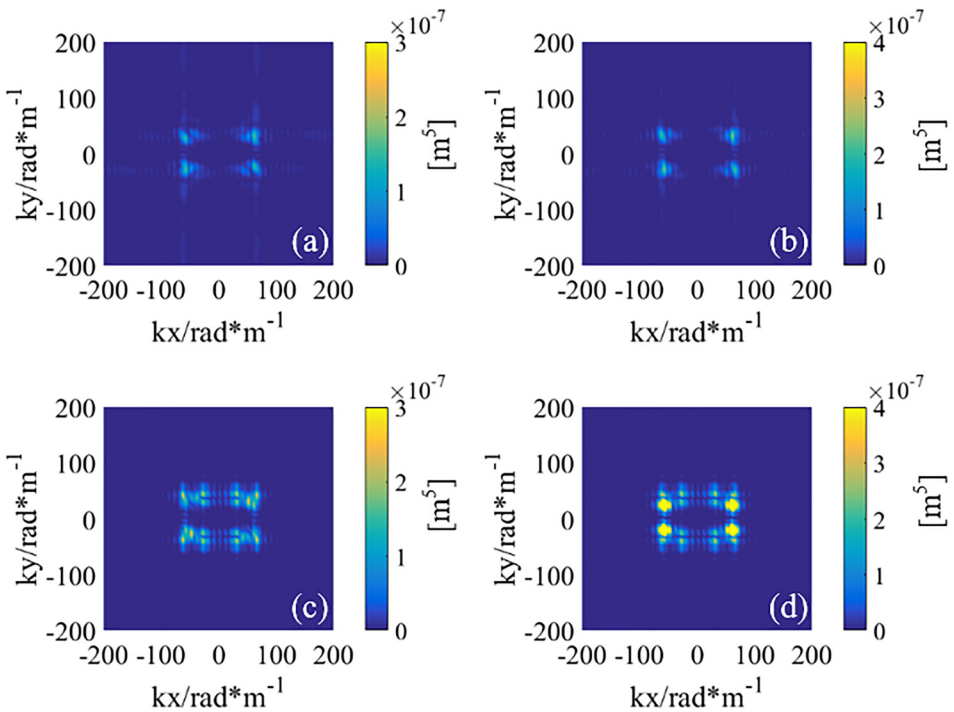

FIG. 11. (Color online) The modulus of wavenumber-domain spectra of cross-correlation function at 4119 Hz. (a) and (b) correspond to the real and imaginary parts, respectively, of ABH plate displacement with acoustic modal vector at interface; (c) and (d) correspond to the real and imaginary parts, respectively, of uniform plate displacement with acoustic modal vector at interface.

an ABH-induced impairment in the structure-acoustic coupling strength, which also explains why the vibration intensity of the ABH-plate is almost the same as those of the uniform plate, but the noise can be significantly reduced. Similarly, the quantitative coupling coefficients of the ABH plate and uniform plate calculated based on Eq. (8) are listed in Table III. The value of $\sqrt{C_1^2+C_2^2}$ of the ABH plate-cavity is 0.15 times that of the uniform plate-cavity, which indicates that the ABH plate exhibits an attractive vibro-acoustic decoupling characteristic.

At the higher frequency of 4119 Hz, close to a modal frequency of the plate, two main effects can be observed in Figs. 10 and 11. The first effect is a significant reduction in the vibration amplitude of the ABH plate because of the

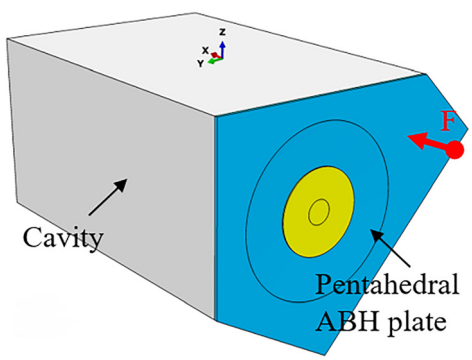

FIG. 12. (Color online) Vibro-acoustic cavity system with the pentagonal ABH plate.

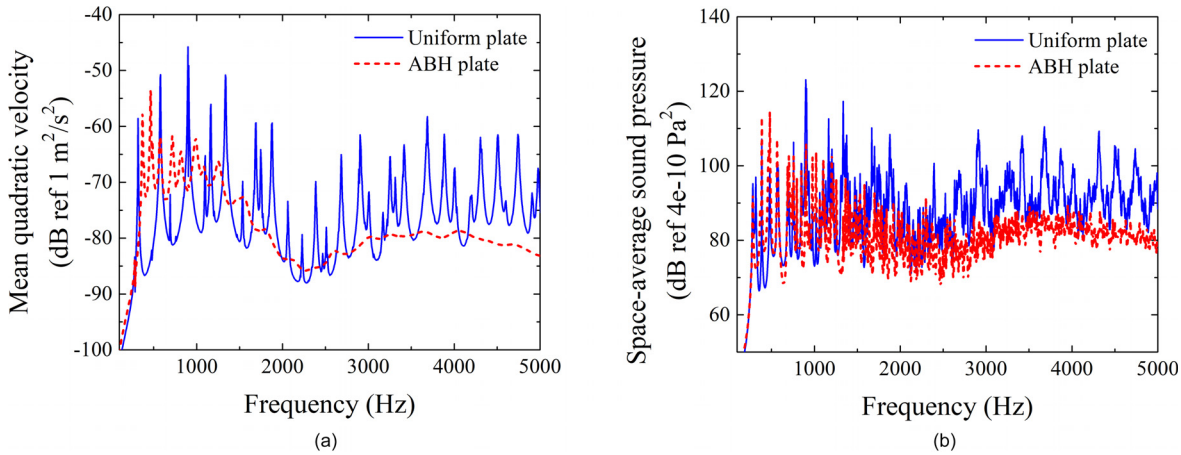

FIG. 13. (Color online) Comparisons between the uniform plate and the ABH plate in narrow band. (a) Mean quadratic velocity of the pentagonal plate. (b) Quadratic space average sound pressure level of the cavity.

ABH-induced damping enhancement, which is basically absent in the uniform plate. The second effect is an increase in the energy at higher wavenumbers, which plays a role in reducing the degree of morphological matching between the plate displacement and the acoustic mode (Fig. 11), similar as at 1309 Hz. Therefore, the ABH effect can not only change the coupling of the vibro-acoustic in the plate-cavity system, but also reduce the vibration energy. The quantitative coupling coefficients are also obtained by Eq. (8), as shown in Table III.

C. Vibro-acoustic decoupling over the irregular pentagonal interface

The effectiveness of the WNDM, as well as the observed phenomena, are revisited using a more general configuration. Using same cavity, the ABH plate is now installed over the other side of the cavity, as shown in Fig. 12, to form an irregular pentagonal interface with a force excitation at (−0.3052, −0.1620, −0.1030).

Figure 13 shows the mean quadratic velocity of the pentagonal plate and the quadratic space-average sound pressure level inside the cavity. As expected, both the structural vibration and cavity noise have been effectively reduced despite the complexity of the interface. Results in Fig. 13 also indicate that a similar mechanism of noise reduction exists regardless of the complexity of the coupling interface.

One representative example of wavelength-domain analysis at 2894 Hz is given to illustrate the damping effect and vibro-acoustic decoupling characteristics of ABH. This frequency, as the resonance frequency of an acoustic mode, is close to a structural mode of the ABH plate at 2889 Hz and a mode of the uniform plate at 2908 Hz, respectively. The mean quadratic velocity is reduced by about 11.3 dB and the space-average sound pressure by 23.6 dB by replacing the uniform plate with the ABH plate. As shown in Eq. (A9), the modal force acting on the considered acoustic mode is proportional to the coupling coefficient, which in turn depends on the degree of morphological matching between the structural modal function and acoustic modal function. Figure 14 shows the structural mode shapes of the two plates and the shape of the corresponding acoustic mode at the plate–cavity interface. Obviously, the shapes of these modes are quite complex so that the degree of morphological matching between those structural modes and the acoustic mode is not straightforward from these graphs. As mentioned before, the proposed WNDM allows a description of the coupling between one acoustic mode with the entire displacement field at the interface, as opposed to the one used before for mode-to-mode coupling.[19]

Figure 15 shows the wavenumber spectra at 2894 Hz. Overall, the results are similar with the data presented in Figs. 8 and 10. However, several new observations are worth noting in Fig. 15. For example, the wavenumber components of the irregular plate are more diverse. Furthermore, it is also noteworthy that the wavenumber spectra of the acoustic modes at the interface have changed significantly. The shape of the spectrum varies greatly, which is in the shape of a bright ring of glowing because the number of modes increases and the coupling is strengthened due to the irregularity of the cavity. Theoretically speaking, the irregularity of the cavity gives rise to higher matching probability for the

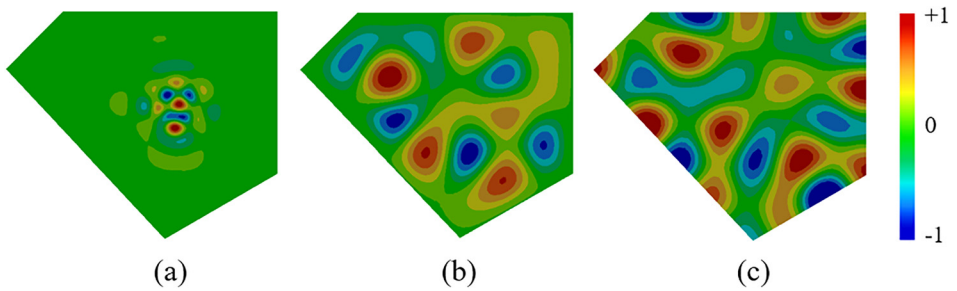

FIG. 14. (Color online) Mode of plate and acoustic mode of the cavity. (a) Mode of the ABH plate at 2889 Hz. (b) Mode of the uniform plate at 2908 Hz. (c) Acoustic mode of the cavity (interface) at 2894 Hz.

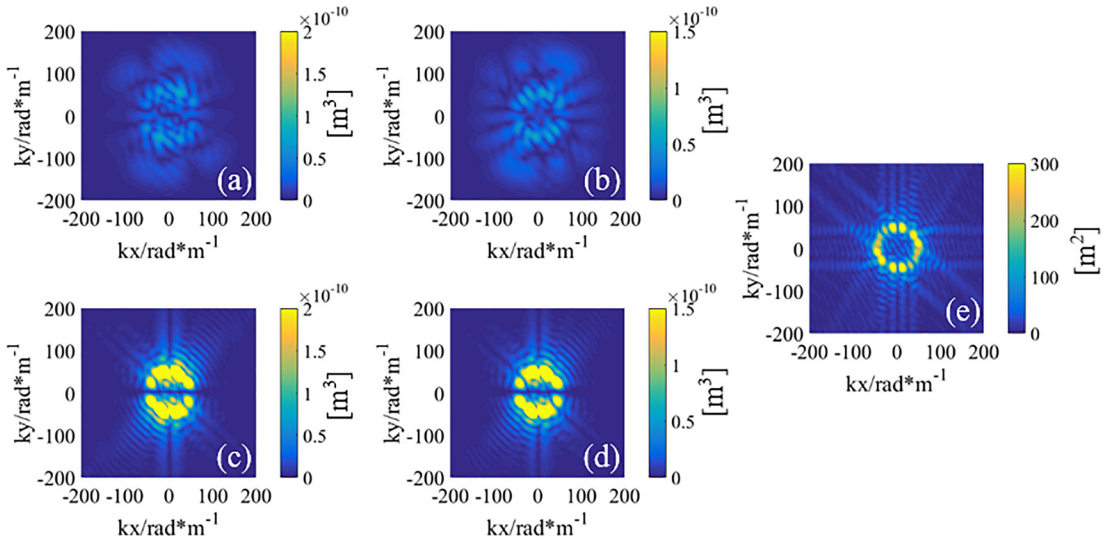

FIG. 15. (Color online) The modulus of wavenumber-domain spectra of the displacements and acoustic mode at 2894 Hz. (a) and (b) correspond to the real and imaginary parts, respectively, of ABH plate displacement; (c) and (d) correspond to the real and imaginary parts, respectively, of uniform plate displacement; (e) corresponds to the acoustic modal vector at the interface.

bending waves in the plate and the acoustic wave in the cavity. In other words, this gives rise to a much more effective coupling between the structure and the enclosure, as shown in Figs. 16(c) and 16(d). However, the matching degree of main wavenumber components between the ABH plate displacement and the acoustic mode is much lower than that between the uniform plate and the cavity, as shown in Fig. 16. The value of the coupling coefficients of the ABH plate-cavity, C_1, C_2, and $\sqrt{CC^*} = \sqrt{C_1^2+C_2^2}$ are 3.39×10^{-8}, 2.27×10^{-8}, and $4.08 \times 10^{+8}$, respectively. Their counterparts for the uniform plate-cavity are 2.89×10^{-7}, 1.84×10^{-7}, and 3.43×10^{-7}, respectively. Obviously, the value of $\sqrt{C_1^2+C_2^2}$ of the ABH plate-cavity is 12% that of the uniform plate-cavity. Therefore, the reason for the noise reduction in the cavity with an ABH plate is the vibration amplitude reduction and mismatching between the displacement spectrum and the spectrum of the acoustic field in the wavenumber domain, which results in a weakened vibro-acoustic coupling. It can be concluded that the ABH structure exhibits the general characteristic of vibro-acoustic decoupling above the cut-on frequency. Meanwhile, the WNDM is useful and effective for the coupling analysis over an irregular interface.

VI. CONCLUSIONS

In this paper, the potential of ABH structures for interior noise reduction in a pentahedral cavity is investigated.

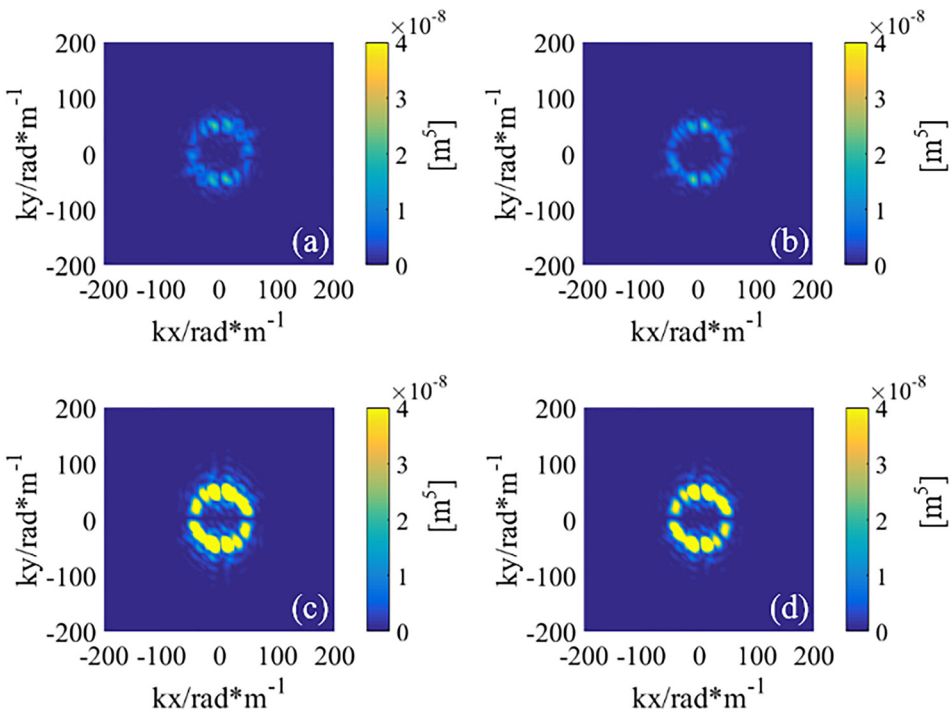

FIG. 16. (Color online) The modulus of wavenumber-domain spectra of cross-correlation function at 2894 Hz. (a) and (b) correspond to real and imaginary parts, respectively, of ABH plate displacement with acoustic modal vector at interface; (c) and (d) correspond to real and imaginary parts, respectively, of uniform plate displacement with acoustic modal vector at interface.

A validated numerical finite element model considering the full plate-cavity coupling is established. The results show the effectiveness of ABH effects on cavity noise reduction, and also demonstrate the potential and benefit of using ABH principles to design lightweight structures. For a better understanding of the vibro-acoustic coupling and observed noise reduction mechanism of the ABH structure, a WNDM is established by deriving the relationship between the space-averaged sound energy inside the cavity and the spectra of the structural displacement and the acoustic mode of the cavity. Using the FE model and the proposed WNDM, two cases are investigated with ABH panels installed on two different facets of the cavity. Results show and confirm a dual physical mechanism behind the noise reduction in the cavity: amplitude reduction and mismatching in the wavenumber spectra between the displacement and the acoustic field, which by the same token weakens its coupling with the enclosed cavity and reduces the sound radiation into the cavity. Results also demonstrate that the proposed WNDM is a useful and effective tool for coupling analysis over an irregular interface, which could further be used for aiding the design, analysis, and optimization of complex ABH vibro-acoustic systems.

ACKNOWLEDGMENTS

This research was supported by the National Natural Science Foundation of China (Grant Nos. 11532006 and 51775267), the Natural Science Foundation of Jiangsu Province (Grant No. BK20181286), Research Grants Council of Hong Kong Special Administrative Region, China (PolyU 152017/17E), Equipment Pre-research Fund (Grant No. 61402100103), Fundamental Research Funds for the Central Universities (Grant No. NE2015001), Six talent peaks project in Jiangsu Province Class C (No. JXQC-002), and a Project Funded by the PAPD. X.W. and H.J. contributed equally to this work.

APPENDIX

The discretized vibro-acoustic coupling equation of the plate-cavity system can be expressed as

$$\begin{bmatrix} M_s & 0 \\ -\rho_0 C & M_a \end{bmatrix} \begin{Bmatrix} \ddot{w} \\ \ddot{p} \end{Bmatrix} + \begin{bmatrix} D_s & 0 \\ 0 & D_a \end{bmatrix} \begin{Bmatrix} \dot{w} \\ \dot{p} \end{Bmatrix} + \begin{bmatrix} K_s & C^T \\ 0 & K_a \end{bmatrix} \begin{Bmatrix} w \\ p \end{Bmatrix} = \begin{Bmatrix} B \\ 0 \end{Bmatrix} F, \tag{A1}$$

where w is the vector of nodal displacement of the plate; p is the vector of nodal sound pressure inside the cavity; ρ_0 is the density of air; M, D, and K are the mass, damping and stiffness matrices for the structure and acoustic field, respectively. C is a matrix representing the coupling between the plate and the acoustic field; F is the excitation force; and B is a vector related to nodal force.

The mean quadratic velocity of the plate and the space-averaged sound energy inside the enclosure are defined as[24]

$$\overline{\langle v_n^2 \rangle} = \frac{1}{2S} \int_S v_n v_n^* dS, \tag{A2}$$

$$\overline{\langle p_e^2 \rangle} = \frac{1}{2V} \int_V p p^* dV, \tag{A3}$$

with v_n being the normal velocity of the plate and S the whole vibrating surface, and V and p are the volume and the acoustic pressure, respectively.

Based on the modal superposition theory, w and p can be decomposed over the *in-vacuum* structural mode shape functions $\varphi = \{\varphi_1, \ldots, \varphi_{n_s}\}^T$ and the rigid-walled acoustic mode shape functions $\psi = \{\psi_1, \ldots, \psi_{n_a}\}^T$, respectively, as

$$w = \varphi q_s = \sum_j q_{sj} \varphi_j, \tag{A4}$$

$$p = \psi q_a = \sum_i q_{ai} \psi_i, \tag{A5}$$

where $q_s = \{q_{s1}, \ldots, q_{sn}\}^T$ and $q_a = \{q_{a1}, \ldots q_{an}\}^T$ are the modal coordinates of the plate and cavity, respectively.

Using the orthogonality property of the modal shape functions and considering the effect of viscous damping, Eq. (A1) can be cast into the following form:

$$\begin{bmatrix} \bar{M}_s & 0 \\ -\rho_0 \bar{C} & \bar{M}_a \end{bmatrix} \begin{Bmatrix} \ddot{q}_s \\ \ddot{q}_a \end{Bmatrix} + \begin{bmatrix} \bar{D}_s & 0 \\ 0 & \bar{D}_a \end{bmatrix} \begin{Bmatrix} \dot{q}_s \\ \dot{q}_a \end{Bmatrix} + \begin{bmatrix} \bar{K}_s & \bar{C}^T \\ 0 & \bar{K}_a \end{bmatrix} \begin{Bmatrix} q_s \\ q_a \end{Bmatrix} = \begin{Bmatrix} \varphi^T B \\ 0 \end{Bmatrix} F, \tag{A6}$$

where $\bar{M}_s$, $\bar{D}_s$, and $\bar{K}_s$ are diagonal matrices of the structural modal mass, damping, and stiffness, respectively, and $\bar{M}_a$, $\bar{D}_a$, and $\bar{K}_a$ are their acoustic counterparts. $\bar{C} = (1/S)\psi^T C \varphi$ is the coupling matrix between the structural modes and acoustic modes.

According to Eqs. (A1) and (A6), the elements in the coupling matrix can be expressed as

$$\bar{C}_{ij} = \frac{1}{S} \psi_i^T C \varphi_j = \frac{1}{S} \int_S \hat{\psi}_i \hat{\varphi}_j \, dx \, dy, \tag{A7}$$

where the modal vector $\hat{\psi}_i$, which only contains the pressure at the interface, is the reduced form of the ith acoustic mode in the cavity, ψ_i, and the modal vectors $\hat{\varphi}_j$, which only includes the normal displacement at the interface, is the reduced form of the jth vibration of mode φ_j. It should be noted that the same symbols have been used for both modal functions in the physical space and modal vectors in discretized space in the above expressions. According to Eq. (A7), it is obvious that the coupling coefficient depends on the morphological matching between the structural modal function and the acoustic modal function at the interface.

Since the damping factor of the acoustic modes is very small, the sound pressure at the acoustic resonance frequencies yields the dominant contribution to the space-average pressure. Therefore, the pressure response at the acoustic resonance frequencies is discussed here by assuming harmonic excitation at the frequency of the ith acoustic mode. According to Eq. (A6), the response of the jth structural mode is

$$q_{sj}(t) = \tilde{q}_{sj} e^{\imath \omega_{ai} t}, \tag{A8}$$

where $\tilde{q}_{sj}$ is the complex amplitude of the structural coordinate, including the initial phase, and $\imath$ is the imaginary unit. The acoustic equation of the system in the modal space can be expressed as

$$\begin{aligned} &\ddot{q}_{ai} + 2\xi_{ai}\omega_{ai}\dot{q}_{ai} + \omega_{ai}^2 q_{ai} \\ &\quad = \frac{\rho_0}{\bar{M}_{ai}} S \sum_j \bar{C}_{ij} \ddot{q}_{sj} = -\frac{\rho_0}{\bar{M}_{ai}} \omega_{ai}^2 \sum_j q_{sj} \int\int \hat{\psi}_i \hat{\varphi}_j \, dx\, dy \\ &\quad = -\frac{\rho_0}{\bar{M}_{ai}} \omega_{ai}^2 e^{\imath \omega_{ai} t} \int\int \tilde{w}_n(x,y) \hat{\psi}_i(x,y) \, dx\, dy, \end{aligned} \tag{A9}$$

where ζ_{ai} and $\bar{M}_{ai}$ are the damping ratio and mass of the ith acoustic mode, respectively, and

$$\tilde{w}_n(x,y) = \sum_j \tilde{q}_{sj} \hat{\varphi}_j(x,y) \tag{A10}$$

is the complex amplitude of the plate vibration at the interface, which includes the initial phase at each position (x,y).

If the response of acoustic modes is expressed as

$$q_{ai}(t) = \tilde{q}_{ai} e^{\imath \omega_{ai} t} = \bar{q}_{ai} e^{\imath(\omega_{ai} t + \phi_{ai})}, \tag{A11}$$

then there exist

$$\bar{q}_{ai} = -\frac{\rho_0}{2\zeta_{ai}\bar{M}_{ai}} C_i, \quad \phi_{ai} = \frac{\pi}{2}, \tag{A12}$$

where

$$C_i = \int\int \tilde{w}_n(x,y) \hat{\psi}_i(x,y) \, dx\, dy \tag{A13}$$

is defined as the coupling coefficient between the acoustic mode and the vibration displacement. It should be noted that this coupling coefficient is a synthetic indicator of the coupling effect between the acoustic mode and all the structural modes at the given frequency.

Because the damping ratio of the acoustic modes is very small, the influence of the non-resonant modes can be neglected. According to Eq. (A5), the acoustic field at the resonance frequency of the ith acoustic mode can be approximately expressed as

$$\tilde{p} = \tilde{q}_{ai} \psi_i(x,y,z), \tag{A14}$$

where $\tilde{q}_{ai}$ is the complex amplitude of the acoustic field defined in Eq. (A11). The quadratic space-averaged sound pressure at the ith acoustic mode is given in the following form:

$$\begin{aligned} \overline{\langle p_e^2 \rangle} &= \frac{1}{2V} \int_V \tilde{p} \tilde{p}^* dv \\ &= \frac{\rho_0^2}{4\zeta_{ai}^2 \bar{M}_{ai}^2} C_i C_i^* \frac{1}{2V} \int\int\int \psi_i^2(x,y,z) \, dx\, dy\, dz, \end{aligned} \tag{A15}$$

where $\int\int\int \psi_i^2(x,y,z) \, dx\, dy\, dz$ is a constant.

[1]V. V. Krylov, "New type of vibration dampers utilising the effect of acoustic 'black holes,' " Acta Acust. Acust. **90**, 830–837 (2004).
[2]V. V. Krylov and R. Winward, "Experimental investigation of the acoustic black hole effect for flexural waves in tapered plates," J. Sound Vib. **300**, 43–49 (2007).
[3]V. V. Krylov, "Acoustic black holes: Recent developments in the theory and applications," IEEE Trans. Ultrason. Ferroelectr. Freq. Control. **61**, 1296–1306 (2014).
[4]L. Tang, L. Cheng, H. Ji, and J. Qiu, "Characterization of acoustic black hole effect using a one-dimensional fully-coupled and wavelet-decomposed semi-analytical model," J. Sound Vib. **374**, 172–184 (2016).
[5]S. C. Conlon and P. A. Feurtado, "Progressive phase trends in plates with embedded acoustic black holes," J. Acoust. Soc. Am. **143**, 921–930 (2018).
[6]J. J. Bayod, "Application of elastic wedge for vibration damping of turbine blade," J. Syst. Des. Dyn. **5**, 1167–1175 (2011).
[7]E. P. Bowyer and V. V. Krylov, "Damping of flexural vibrations in turbofan blades using the acoustic black hole effect," Appl. Acoust. **76**, 359–365 (2014).
[8]V. Georgiev, J. Cuenca, F. Gautier, L. Simon, and V. Krylov, "Damping of structural vibrations in beams and elliptical plates using the acoustic black hole effect," J. Sound Vib. **330**, 2497–2508 (2011).
[9]E. P. Bowyer, D. J. O'Boy, V. V. Krylov, and F. Gautier, "Experimental investigation of damping flexural vibrations in plates containing tapered indentations of power-law profile," Appl. Acoust. **74**, 553–560 (2013).
[10]E. P. Bowyer and V. V. Krylov, "Experimental study of sound radiation by plates containing circular indentations of power-law profile," Appl. Acoust. **88**, 30–37 (2015).
[11]S. C. Conlon, J. B. Fahnline, and F. Semperlotti, "Numerical analysis of the vibroacoustic properties of plates with embedded grids of acoustic black holes," J. Acoust. Soc. Am. **137**, 447–457 (2015).
[12]P. A. Feurtado and S. C. Conlon, "Wavenumber transform analysis for acoustic black hole design," J. Acoust. Soc. Am. **140**, 718–727 (2016).
[13]X. Li and Q. Ding, "Sound radiation of a beam with a wedge-shaped edge embedding acoustic black hole feature," J. Sound Vib. **439**, 287–299 (2019).
[14]L. Ma and L. Cheng, "Sound radiation and transonic boundaries of a plate with an acoustic black hole," J. Acoust. Soc. Am. **145**, 164–172 (2019).
[15]E. H. Dowell and H. M. Voss, "The effect of a cavity on panel vibration," AIAA J. **1**, 476–477 (1963).
[16]E. H. Dowell, G. F. Gorman, and D. A. Smith, "Acoustoelasticity: General theory, acoustic natural modes and forced response to sinusoidal excitation, including comparisons with experiment," J. Sound Vib. **52**, 519–542 (1977).
[17]Y. Y. Li and L. Cheng, "Vibro-acoustic analysis of a rectangular-like cavity with a tilted wall," Appl. Acoust. **68**, 739–751 (2007).
[18]M. C. Junger and D. Feit, *Sound, Structures, and Their Interaction* (MIT Press, Cambridge, MA, 1986).
[19]H. Ji, X. Wang, J. Qiu, L. Cheng, Y. Wu, and C. Zhang, "Noise reduction inside a cavity coupled to a flexible plate with embedded 2-D acoustic black holes," J. Sound Vib. **455**, 324–338 (2019).
[20]L. Zhao, S. C. Conlon, and F. Semperlotti, "Broadband energy harvesting using acoustic black hole structural tailoring," Smart Mater. Struct. **23**, 065021 (2014).
[21]W. Huang, H. Ji, J. Qiu, and L. Cheng, "Wave energy focalization in a plate with imperfect two-dimensional acoustic black hole indentation," J. Vib Aoust. **138**, 061004 (2016).
[22]P. A. Feurtado and S. C. Conlon, "An experimental investigation of acoustic black hole dynamics at low, mid, and high frequencies," J. Vib Acoust. **138**, 061002 (2016).
[23]L. Tang and L. Cheng, "Enhanced acoustic black hole effect in beams with a modified thickness profile and extended platform," J. Sound Vib. **391**, 116–126 (2017).
[24]L. Cheng and J. Nicolas, "Radiation of sound into a cylindrical enclosure from a point-driven end plate with general boundary conditions," J. Acoust. Soc. Am. **91**, 1504–1513 (1992).